Low-temperature annealing behavior of defects in Mg-ion-implanted GaN studied using MOS diodes and monoenergetic positron beam

Masamichi Akazawa[1,*], Ryo Kamoshida[1], Shunta Murai[1], Tetsu Kachi[2], and Akira Uedono[3]

[1]*Research Center for Integrated Quantum Electronics, Hokkaido University, Sapporo, Hokkaido 060-0813, Japan*

[2]*Institute of Materials and Systems for Sustainability, Nagoya University, Nagoya, Aichi 464-8601, Japan*

[3]*Division of Applied Physics, Faculty of Pure and Applied Science, University of Tsukuba, Tsukuba, Ibaraki 305-8573, Japan*

E-mail: akazawa@rciqe.hokudai.ac.jp

Mg ions were implanted into Si-doped (5×10^{17} cm^{-3}) n-GaN at a dose of 1.5×10^{11} or 1.5×10^{12} cm^{-2}. MOS diodes were used to characterize the implanted GaN after 300 ℃ annealing for 3 h and after additional 500 ℃ annealing for 3 min. Although capacitance–voltage (*C–V*) characteristics varied with the dosage, the effects of acceptor-like defects induced by ion implantation were observed in the *C–V* characteristics independently of dosage and annealing temperature. A defect level at approximately 0.25 eV below the conduction band edge was detected electrically. By positron annihilation spectroscopy, its origin was identified as a divacancy consisting of Ga and N vacancies. It was found that its density compared with that of as-implanted GaN decreased with 300 ℃ annealing, and further increased with 500 ℃ annealing. This phenomenon was explained on the basis of the difference between the diffusion barriers of possible point defects.

1. Introduction

GaN has revolutionized optoelectronics with the introduction of high-brightness light-emitting diodes[1, 2]. Recently, this material has attracted attention as a promising material for power devices[3–5] because of its wide bandgap[5], high breakdown field[6], good thermal conductivity[5], high electron mobility at low electric fields[5], and high electron saturation velocity at high electric fields[7]. In addition, an excellent metal-oxide-semiconductor (MOS) structure with a thoroughly minimized interface state density can be obtained by carefully depositing an insulator on a GaN surface[8–11], which leads to the realization of high-efficiency power devices, such as vertical MOS field-effect transistors[4, 12–14]. In the fabrication of power devices, ion implantation is a convenient method for forming a selectively doped region as a building block. However, for GaN, ion implantation for forming a p-type region has been difficult.

Recently, p-type conductivity has been reported to be achieved by Mg ion implantation combined with high-temperature annealing to activate Mg acceptors and recover defects. Rapid thermal annealing (RTA) with sequential pulse heating, named multicycle RTA, has been reported to be efficient for activating Mg acceptors[15–18]. Although this method was carried out under a nitrogen overpressure of 2 MPa, it has been reported that a p-type region can be obtained by Mg ion implantation combined with annealing at a temperature higher than 1230 °C even in atmospheric-pressure nitrogen[19–22]. However, the activation rate seems to be higher for annealing under the nitrogen overpressure. Moreover, ultrahigh-pressure annealing in which Mg-ion-implanted GaN was annealed at 1400 °C or higher under a nitrogen overpressure of 1 GPa was performed, resulting in a successful generation of holes confirmed by the temperature dependence of the Hall effect with a high activation ratio[23].

In addition to obtaining a p-type region successfully, defect levels generated by Mg ion implantation have also been investigated. Deep-level transient spectroscopy (DLTS) using Schottky barrier diodes revealed several defect levels at 0.2–1.1 eV below the conduction band edge E_C in Mg-ion-implanted GaN after annealing at various temperatures up to 1000 °C[24]. Another approach has been used for the electrical measurement of defect levels using a MOS structure with Mg-ion-implanted GaN[25–27]. Both approaches were used for evaluating lightly Mg-ion-implanted GaN that exhibited n-type conduction, which enabled the comparison of the results with a vast amount of previously reported data on defect levels detected in n-type GaN[28–36]. Nevertheless, the assignment of defects by a method other than electrical measurements has not been performed to investigate the effects of low-temperature annealing on Mg-ion-implanted GaN.

On the other hand, positron annihilation spectroscopy (PAS) is a powerful method for analyzing vacancy defects in various materials. This method has been applied to Mg-ion-implanted GaN[37–40]. On the basis of the results of PAS for room-temperature Mg ion implantation, the Ga–N divacancy ($V_{Ga}V_N$) was mainly detected for as-implanted samples[38]. Upon annealing at 1000 ºC, vacancy agglomeration occurred to form vacancy clusters. It was suggested that vacancy defects existed even after annealing at 1300 ºC, which can cause carrier trapping and scattering. Such defects may lower the activation rate of Mg and affect the device performance. To realize a power device with excellent performance, methods of controlling defects should be developed. Although high-temperature annealing cannot eliminate defects completely, a clue to developing a method of controlling defects might be obtained by investigating the behavior of defects generated by ion implantation upon low-temperature annealing.

In this study, we investigate the behavior of defects generated by Mg ion implantation upon annealing at 300 and 500 ºC by a combination of electric measurement using MOS diodes and analysis using a monoenergetic positron beam. In addition to the Ga vacancy (V_{Ga}) and its clusters with the N vacancy (V_N), we also discuss the behavior of interstitial Ga (Ga_i) and interstitial N (N_i).

2. Experimental procedure

Samples were prepared as shown in Fig. 1 and as described below. A Si-doped n-GaN layer (3 μm thick, $n = 5\times10^{17}$ cm^{-3}) was grown on a free-standing n$^+$-GaN (0001) substrate via an n$^+$-GaN buffer layer by metalorganic vapor phase epitaxy (MOVPE). Mg ions were implanted at room temperature at an energy of 50 keV, an angle of 7º, and a dose of 1.5×10^{11} or 1.5×10^{12} cm^{-2}. The depth profiles of the Mg concentration, [Mg], were measured by secondary ion mass spectroscopy (SIMS). Figure 2 shows the SIMS [Mg] profile for the as-implanted low-Mg-ion-dose sample in comparison with the calculation results obtained using the "stopping and range of ions in matter (SRIM)" code for [Mg], the concentration of V_{Ga}, [V_{Ga}], and that of V_N, [V_N]. The calculated [Mg] is in good agreement with the SIMS result at the top of the profile, although the tail in the SIMS profile indicated a trace of the channeling phenomenon. Note that high [V_{Ga}] and [V_N] are calculated. Since the vacancies are accompanied by interstitials, the concentrations of Ga_i and N_i can be in a similar order to [V_{Ga}] and [V_N]. Therefore, we can expect the detection of the defects produced by implantation. Thereafter, for the samples with 500 ºC annealing, a 20-nm-thick Al_2O_3 layer was formed by atomic layer deposition (ALD) using trimethylaluminum and H_2O at a

substrate temperature of 300 ºC, followed by annealing at 500 ºC for 3 min under nitrogen flow and the removal of the Al_2O_3 layer. For the sample without 500 ºC annealing, this process step was not carried out. The fabrication of MOS diodes was completed by forming a 30-nm-thick Al_2O_3 layer by ALD, followed by the metallization of a Ni/Au electrode on the top and an ohmic contact of Ti/Au on the back surface of the GaN substrate. Finally, postmetallization annealing (PMA) was carried out for 3 h at 300 ºC in air to reduce the interface state density (D_{it})[8, 9]. For the completed MOS diodes, capacitance–voltage (*C–V*) and capacitance–frequency (*C–f*) measurements were carried out. The bare GaN samples for PAS analysis were prepared by removing the Al_2O_3 layer after the same annealing steps as those for the MOS diodes to ensure the same thermal history.

Although details on PAS were described previously[37–40], a brief explanation of PAS is as follows. Upon the annihilation of a positron, a γ-ray is radiated with an energy of 511 keV. When the annihilation is induced by a vacancy defect, the line width of the radiated γ-ray compared with that in the defect-free (DF) case undergoes Doppler broadening. The line-shape parameter *S* is defined as the ratio of the integrated intensity in the range of 510.22–511.78 keV to the total integrated intensity, whereas the wing parameter *W* is the fraction of the integrated intensity in the ranges of 504.14–507.96 and 514.04–517.86 keV. By measuring *S* at various positron energies, we obtained the depth profile of *S* increased by the vacancy defects. The relationship between *S* and positron energy was analyzed using VEPFIT, a computer program developed by van Veen et al.[41] Moreover, by coincidence Doppler broadening (CDB) measurement, where *S* and *W* are measured coincidentally, we can assign a defect by comparison with the theoretically calculated *S–W* relations for possible vacancy defects. The Doppler broadening spectra of positrons corresponding to the annihilation of positrons were calculated using the quantum materials simulator (QMAS) code. This program adopts the projector augmented-wave (PAW) method[42] to obtain electron wave functions. Details of the calculation procedure are described elsewhere.[43]

3. Results and discussion

3.1 Electrical properties of MOS diodes

In the case of the lower Mg ion dose, the MOS diodes with 300 ºC annealing exhibited anomalous *C–V* characteristics as shown in Fig. 3(a), where the bias voltage was swept from the negative side to the positive side. Here, the ideal curve assuming no implantation was calculated with the same flat-band-voltage shift as the experimental *C–V* curve of the MOS diode with unimplanted n-GaN. Around zero bias, the slope of the *C–V* curve is steeper than

that of the ideal curve. In addition, a plateau can be seen distinctly. These results indicate that defects existed in the bulk of the Mg-ion-implanted GaN. In particular, the anomalously steep region appearing on the right side of the ideal curve indicates that an acceptor-like defect compensating for the Si donor existed predominantly in GaN[44, 45]. Furthermore, a slight frequency dispersion was observed. Although the frequency dispersion and the plateau of the *C–V* characteristics were reduced by 500 ºC annealing as shown in Fig. 3(b), the anomalously steep region still existed, indicating that the acceptor-like bulk defect persisted.

Since the measured *C–V* curves are affected by the acceptor-like defect being partially steeper than the ideal curve, the high-frequency capacitance method for deriving the interface state density D_{it} cannot be applied to the 1 MHz *C–V* curves in Figs. 3(a) and 3(b). Instead, we applied the high-low-frequency capacitance method to 1 MHz and 1 kHz *C–V* curves. In this method, D_{it} is derived from the high-frequency-limit capacitance C_{HF} and the low-frequency-limit capacitance C_{LF} according to[46]

$$D_{it} = \frac{1}{q^2}\left(\left(\frac{1}{C_{LF}} - \frac{1}{C_{OX}}\right)^{-1} - \left(\frac{1}{C_{HF}} - \frac{1}{C_{OX}}\right)^{-1}\right), \quad (1)$$

where C_{OX} is the oxide capacitance. Here, the position of the surface Fermi level E_{FS} corresponding to V was calculated by[46]

$$E_C - E_{FS} = \int_{V_0}^{V}\left(1 - \frac{C_{LF}}{C_{OX}}\right)dV, \quad (2)$$

where V_0 is the voltage for strong accumulation. Regarding the 1 kHz and 1 MHz capacitances as C_{LF} and C_{HF}, respectively, we derived the D_{it} distribution in the range near E_C where the time constants of the interface states are sufficiently small. The result is shown in Fig. 4. Here, the detected traps are assigned to not only the interface states but also the bulk traps as discussed later. Therefore, the derived density distribution should be labeled as the trap density D_T distribution. A discrete level seems to exist at around E_C – 0.25 eV for the sample annealed at 300 ºC. For the sample annealed at 500 ºC, this level may be merged with the near-E_C edge of the continuous interface state density distribution having a U shape over the entire band gap. It can be seen that the D_T distribution at the energy position deeper than E_C – 0.3 eV disappeared after 500 ºC annealing, which might have led to the reduction in the frequency dispersion and that in the plateau length of *C–V* curves.

With an increase in Mg ion dose, the *C–V* characteristics changed markedly. As shown

in Fig. 5(a), a marked frequency dispersion was observed. In addition, a long plateau was also observed in the negative bias region. Although the length of the plateau was decreased by 500 ºC annealing during MOS diode fabrication as shown in Fig. 5(b), the severity of frequency dispersion was not diminished markedly. To investigate the frequency dispersion in detail, *C–f* measurement was carried out. The obtained characteristics are shown in Figs. 6(a) and 6(b) for the 300-ºC-annealed and 500-ºC-annealed samples, respectively, which showed very similar characteristics. This type of frequency dispersion was caused by strong Fermi level pinning.

There is a possibility that the observed Fermi level pinning was caused by the Al_2O_3/GaN interface states. To examine this possibility, the *C–f* characteristics were analyzed. The interface state conductance G_p/ω can be obtained as[46)]

$$\frac{G_p}{\omega} = \frac{C_{OX}^2\left(G_m/\omega\right)}{\left(G_m/\omega\right)^2 + (C_{OX} - C_m)^2}, \tag{3}$$

where ω is the angular frequency, C_m is the measured capacitance, and G_m is the measured conductance. The analysis results are shown in Figs. 7(a) and 7(b) for the 300-ºC-annealed and 500-ºC-annealed samples, respectively, which show that the frequency range where the conductance peak was detected was not affected by the annealing temperature. In these figures, the solid circles show experimental data, whereas the solid lines are fitted lines, assuming a single time constant τ, according to[46)]

$$\frac{G_p}{\omega} = \frac{\omega\tau}{1+\omega^2\tau^2} C_{it}, \tag{4}$$

where C_{it} is the interface state capacitance. The experimental data are well fitted by the single-time-constant model, which indicates that the interface states have single time constants. This seems to be unusual because, in a typical case, the time constants of the interface states cannot be determined singly and they distribute in a certain range. D_{it} was derived as[46)]

$$D_{it} = \frac{C_{it}}{q^2}, \tag{5}$$

where q is the elementary charge. To obtain the D_T distribution in the band gap, the bias

voltage V that varies the surface potential ψ_S was changed as indicated in Figs. 6 and 7. ψ_S corresponding to each V can be derived from the high-frequency-limit C–V curve, which leads to the determination of the energy position of the detected interface states. However, the high-frequency-limit C–V curve was not achieved in the present data. On the other hand, the energy E_T of an electron trap is related to the electron emission time constant corresponding to τ as[24, 28, 35)]

$$\tau = \frac{1}{\sigma v_{th} N_C} exp\left(\frac{E_C - E_T}{kT}\right), \quad (6)$$

where σ is the capture cross section of the interface state, v_{th} is the thermal velocity of electrons, N_C is the density of states at E_C, k is the Boltzmann constant, and T is the temperature. Here, $E_C - E_T$ was determined by solving Eq. (6) assuming σ to be 1×10^{-16} cm^{-2} with reference to the previous results of the DLTS study of defect levels in GaN[32)].

The D_T distributions derived from G_p/ω peaks are shown in Fig. 8 for the two annealing temperatures considered. A very similar discrete level at around $E_C - E_T$ = 0.25 eV was derived clearly for both annealing temperatures, which also means that the surface Fermi level was pinned at around E_C – 0.25 eV by this level despite the large bias change. According to the disorder-induced-gap-state model that is a guiding principle concerning the origin of interface states, the D_T distribution should have a U shape in the entire band gap[47, 48)]. However, a discrete level can be detected when high-density bulk defects exist in the vicinity of the semiconductor surface[49, 50)]. Therefore, the detected discrete level should have been the bulk defect level. The same discussion can be applied to the D_T distribution derived for the low-Mg-ion-dose sample as shown in Fig. 3. A similar defect level was previously reported to be observed at around $E_C - E$ = 0.25 eV[28–30, 32–34, 36)]. According to the literature, this defect level can be assigned to the divacancy $V_{Ga}V_N$[29, 30, 32, 34)] that is an acceptor-like defect. Moreover, without the compensation for the Si donor in the GaN bulk, the capacitance at the deep depletion plateau of the C–V curves cannot be achieved by band bending with the surface Fermi level pinning at around E_C – 0.25 eV. Therefore, the donor compensation by an acceptor defect should have been present inside the n-GaN layer or the acceptor defect should have distributed in the GaN bulk.

3.2 Analysis using monoenergetic positron beam

As described above, the C–V characteristics were highly likely affected by an acceptor-like defect independent of the dose and annealing conditions. Moreover, a possibility of the

generation of $V_{Ga}V_N$ was indicated. However, the assignment of defect by electrical measurement is indirect. To examine the acceptor-like vacancy defect directly, PAS was performed. The positron energy dependence of *S* is plotted for the low-Mg-ion-dose sample in Fig. 9(a) and the high-Mg-ion-dose sample in Fig. 9(b) with the variation in annealing temperature. In these figures, the mean implantation depth of positrons is also indicated at the top. DF GaN exhibits an *S* of 0.441[37]. The observed larger *S* values indicate the existence of vacancy defects in Mg-ion-implanted GaN. *S* increases monotonically toward the surface and with the dose. In Figs. 9(a) and 9(b), the solid lines are fitted curves with the *S* parameter profiles as indicated in Figs. 10(a) and 10(b), respectively. In Figs. 10(a) and 10(b), the depth profiles of [Mg] measured by SIMS are also shown. For fitting, the region probed by positrons was divided into three blocks. The first and second blocks are damaged regions, and the third block is the DF region. It can be seen that *S* is high in the region within 70 nm from the surface and is low in the deeper region of GaN. Note that the high *S* was observed in the near-surface region where the *C–V* characteristics of the MOS diodes are mainly affected. Independently of the dose, *S* decreases after 300 ºC annealing and increases after additional 500 ºC annealing, although it is highest in the as-implanted sample.

For the defect assignment, CDB measurement was performed. The obtained *S–W* plot for the low-Mg-ion-dose sample is shown in Fig. 11(a) and that for the high-Mg-ion-dose sample is shown in Fig. 11(b). In both figures, the brown DF data point was obtained for the unimplanted GaN[39]. In Figs. 11(a) and 11(b), the data for the as-implanted GaN and 300- and 500-ºC-annealed samples are all along the broken line connecting the DF and $V_{Ga}V_N$ points. Therefore, $V_{Ga}V_N$ was detected mainly, without causing agglomeration in the temperature range considered for both Mg ion doses. The assignment of the $E_C - 0.25$ eV defect level detected by electrical measurement to $V_{Ga}V_N$ seems to be reasonable considering these results. It can be seen that the (*S, W*) point after 300 ºC annealing locates closer to the DF (*S, W*) point than that for the as-implanted GaN. After 500 ºC annealing, however, the (*S, W*) point shifts slightly away from the DF (*S, W*) point. In Fig. 11(b) for the high-Mg-ion-dose sample, each (*S, W*) point shifted toward the lower right compared with that in Fig. 11(a) for the low-Mg-ion-dose sample. This difference should have resulted mainly from the increase in defect density with the dose. Note that for both Mg ion doses, the (*S, W*) point locates closer to the DF data point upon 300 ºC annealing, indicating a decrease in the density of $V_{Ga}V_N$.

3.3 Possible diffusion of defects

The S parameter increased and decreased upon 300 ºC and 500 ºC annealing, respectively, independent of the Mg ion dose. In the following, we outline the mechanism of the observed phenomenon by considering the diffusion of simple defects.

The diffusion coefficient D is expressed as

$$D = D_0 exp\left(-\frac{E_A}{kT}\right), \quad (7)$$

where D_0 is the frequency factor and E_A is the activation energy. Generally, E_A is given by the sum of the migration barrier E_M and formation energy of defects. However, E_A is equal to E_M when a nonequilibrium density of defects exists in GaN[51], which applies to the present case for the implanted samples. According to previous reports[51–56], there is a tendency in the magnitude order of E_M of simple defects, including interstitial Mg (Mg_i), in n-GaN to be V_N > Mg_i > V_{Ga} > N_i > Ga_i. On the other hand, in n-GaN, the ionized states of these defects are considered to be V_N^+, Mg_i^{2+}, V_{Ga}^{2-} or V_{Ga}^{3-}, N_i^-, and Ga_i^{2+} or Ga_i^{+} [56, 57]. Since $V_{Ga}V_N$ has a negative charge, Ga_i likely combines with $V_{Ga}V_N$ to reduce its density, whereas N_i seems to seldom combine because of the Coulomb repulsion. Since D_0 has not been measured for each defect, a quantitative discussion is difficult. In the following, we will make a qualitative discussion.

A change in defect concentration caused by diffusion can be discussed on the basis of the magnitude relation among E_M of simple defects. In the present temperature range, it is difficult for V_N to be mobile[52], and $V_{Ga}V_N$ is also considered to be immobile on the basis of a previous PAS study[38]. Since Ga_i becomes mobile even at 300 ºC[55], some $V_{Ga}V_N$ defects should have been transformed into V_N by Ga_i upon 300 ºC annealing independent of the dose. It is likely that this phenomenon was observed by PAS as a decrease in S after 300 ºC annealing, compared with that for the as-implanted GaN shown in Figs. 9 and 10. Moreover, there is a possibility that V_{Ga} cannot be mobile upon 300 ºC annealing but can be mobile upon 500 ºC annealing, which likely resulted in a situation where V_{Ga} and V_N did not combine upon 300 ºC annealing but combined to form $V_{Ga}V_N$ upon 500 ºC annealing. This can be the reason why S increased upon 500 ºC annealing. (E_M of Mg_i is higher than that of V_{Ga}. In addition, [Mg] should have been well below the concentrations of other defects on the basis of the SRIM results, as shown in Fig. 2, and the discussion in the next subsection. Therefore, we believe that the diffusion of Mg_i can be ignored.)

3.4 Electrical properties revisited

The dose-dependent differences in *C*–*V* characteristics should have resulted from the difference in Fermi level pinning. The frequency dispersion observed for the sample with the dose of 1.5×10^{12} cm^{-2} was caused by strong Fermi level pinning. Usually, this degree of pinning is caused by D_T larger than 5×10^{13} cm^{-2}eV^{-1}. The reason for this is shown in Figs. 12(a) and 12(b), where $d\psi_S/V$ and C_{LF} are calculated as functions of D_T, respectively, according to[46)]

$$\frac{d\psi_S}{dV} = \left(\frac{C_D+q^2D_T}{C_{OX}} + 1\right)^{-1}, \tag{8}$$

and

$$C_{LF} = \left(\frac{1}{C_{OX}} + \frac{1}{C_D+q^2D_T}\right)^{-1}, \tag{9}$$

where C_D is the depletion capacitance and C_{OX} was assumed to be 2.5×10^{-7} F/cm^2. When D_T is larger than 5×10^{13} cm^{-2}eV^{-1}, $d\psi_S/dV$ becomes smaller than 30 meV independent of C_D, and C_{LF} becomes large close to C_{OX} also independent of C_D, as shown in Figs. 12(a) and 12(b), respectively. In Figs. 5(a) and 5(b), the measured *C* becomes closer to C_{OX} on the low frequency side. Actually, D_T larger than this value was observed for the high-Mg-ion-dose sample as shown in Fig. 6. As has been shown in Fig. 3, the reduction in Mg ion dose led to a reduction in D_T by more than one order, which resulted in the absence of strong Fermi level pinning.

For both Mg-ion-dose samples, the defect level at around E_C – 0.25 eV was detected. The D_T of this defect was higher for the high-Mg-ion-dose sample than for the low-Mg-ion-dose sample. Moreover, the high-Mg-ion-dose sample exhibited higher *S* parameters than the low-Mg-ion-dose sample, which indicated that the concentration of $V_{Ga}V_N$, [$V_{Ga}V_N$], was higher for the high-Mg-ion-dose sample. Therefore, it is reasonable to assign the defect level observed at around E_C – 0.25 eV to $V_{Ga}V_N$ as in many DLTS studies[29, 30, 32, 34)].

The difference in the magnitude of D_T of $V_{Ga}V_N$ between the low- and high-Mg-ion-dose samples in Figs. 4 and 8 was two orders despite the one-order difference in Mg ion dose. The reason for this can be explained as follows. On the basis of *C*–*V* characteristics, the depletion widths with E_{FS} at E_C – 0.25 eV were ~10 and ~100 nm for the low- and high-Mg-ion-dose samples, respectively. Since D_T for the bulk defect levels can be roughly given by the product of the depletion width and the defect concentration, the average [$V_{Ga}V_N$] can

be estimated to be on the orders of 10^{17} and 10^{18} cm^{-3} for the low- and high-Mg-ion-dose samples, respectively.

4. Conclusions

By the combined use of the electrical measurement using MOS diodes and PAS, we investigated the low-temperature annealing behavior of defects in Mg-ion-implanted GaN. Mg ions were implanted into Si-doped (5×10^{17} cm^{-3}) n-GaN at a dose of 1.5×10^{11} or 1.5×10^{12} cm^{-2}. The fabrication of MOS diodes included 300 ºC annealing. An additional 500 ºC annealing was examined. PAS was performed for the samples with the same annealing conditions and also for the as-implanted sample. Although the *C–V* characteristics changed depending on the Mg ion dose, the effects of an acceptor-like defect were indicated independent of the dose and annealing conditions. For the low-Mg-ion-dose sample, the D_T distribution derived by the high-low-capacitance method contained a discrete level around E_C – 0.25 eV. By applying the conductance method to the analysis of the *C–f* characteristics of the high-Mg-ion-dose sample that exhibited strong Fermi level pinning, the defect level around E_C – 0.25 eV was detected more distinctly. Moreover, $V_{Ga}V_N$ was mainly detected by PAS independent of the annealing conditions and Mg ion dose. Therefore, the assignment of the detected defect level around E_C – 0.25 eV to $V_{Ga}V_N$ is reasonable. The density of $V_{Ga}V_N$ was decreased by 300 ºC annealing compared with that of the as-implanted GaN, whereas it was increased by an additional 500 ºC annealing. We consider that the diffusion of Ga_i upon 300 ºC annealing and that of V_{Ga} upon 500 ºC annealing might have decreased and increased the density of $V_{Ga}V_N$, respectively.

Acknowledgments

The authors thank Dr. T. Narita of Toyota Central R&D Labs., Inc. for the MOVPE growth of GaN epitaxial layers and for fruitful discussions. This work was supported by MEXT “Research and development of next-generation semiconductor to realize energy-saving society” Program Grant Number JPJ005357.

References

1) H. Amano, M. Kito, K. Hiramatsu and I. Akasaki, Jpn. J. Appl. Phys. **28**, L2112 (1989).
2) S. Nakamura, T. Mukai and M. Senoh, Appl. Phys. Lett. **64**, 1687 (1994).
3) T. Kachi, Jpn. J. Appl. Phys. **53**, 100210 (2014).
4) H. Amano et al., J. Phys. D, Appl. Phys. **51**, 163001 (2018).
5) D. Ueda, in *Power GaN Devices*, eds. M. Meneghini, G. Meneghesso, and E. Zanoni, (Springer, New York, 2017), Ch. 1.
6) B. J. Baliga, Semicond. Sci. Technol. **28**, 074011 (2013).
7) F. Schwierz, Solid-State Electronics **49**, 889 (2005).
8) S. Kaneki, J. Ohira, S. Toiya, Z. Yatabe, J. T. Asubar, T. Hashizume, *Appl. Phys. Lett.* **109**, 162104 (2016).
9) T. Hashizume, S. Kaneki, T. Oyobiki, Y. Ando, S. Sasaki, and K. Nishiguchi, Appl. Phys. Express **11**, 124102 (2018).
10) T. Yamada, D. Terashima, M. Nozaki, H. Yamada, T. Takahashi, M. Shimizu, A. Yoshigoe, T. Hosoi. T. Shimura, H. Watanabe, Jpn. J. Appl. Phys. **58**, SCCD06 (2019).
11) T. Nabatame, E. Maeda, M. Inoue, K. Yuge, M. Hirose, K. Shiozaki, N. Ikeda, T. Ohishi, and A. Ohi, Applied Physics Express **12**, 011009 (2019).
12) T. Oka, T. Ina, Y. Ueno, J. Nishi, Appl. Phys. Express **8**, 054101 (2015).
13) D. Ji, A. Agwal, H. Li, W. Li, S. Keller, S. Chowdhury, IEEE Electron Dev. Lett. **39**, 863 (2018).
14) D. Ji, W. Li, A. Agwal, S. H. Chan, J. Haller, D. Bisi, M. Labrecque, C. Gupta, B. Cruse, R. Lal, S. Keller, U. K. Mishra, S. Chowdhury, IEEE Electron Dev. Lett. **39**, 1030 (2018).
15) B. N. Feigelson, T. J. Anderson, M. Abraham, J. A. Freitas, J. K. Hite, C. R. Eddy, F. J. Kub, J. Cryst. Growth **350**, 21 (2012).
16) T. J. Anderson, B. N. Feigelson, F. J. Kub, M. J. Tadjer, K. D. Hobart, M. A. Mastro, J. K. Hite, C. R. Eddy, Electron. Lett. **50**, 197 (2014).
17) J. D. Greenlee, T. J. Anderson, B. N. Feigelson, K. D. Hobart, F. J. Kub, Phys. Status Solidi A **212**, 2772 (2015).
18) T. J. Anderson, J. D. Greenlee, B. N. Feigelson, J. K. Hite, K. D. Hobart, F. J. Kub, IEEE Trans. Semicond. Manuf. **29**, 343 (2016).
19) K. Nomoto, K. Takahashi, T. Oikawa, H. Ogawa, T. Nishimura, T. Mishima, H. G. Xing, T. Nakamura, ECS Trans. **69**, 105 (2015).
20) T. Oikawa, Y. Saijo, S. Kato, T. Mishima, T. Nakamura, Nuclear Instruments and Methods in Physics Research B **365**, 168 (2015).

21) T. Narita, T. Kachi, K. Kataoka, T. Uesugi, Appl. Phys. Exp. **10**, 016501 (2017).
22) T. Niwa, T. Fujii, T. Oka, Appl. Phys. Express **10**, 091002 (2017).
23) H. Sakurai, M. Omori, S. Yamada, Y. Furukawa, H. Suzuki, T. Narita, K. Kataoka, M. Horita, M. Bockowski, J. Suda, and T. Kachi, Appl. Phys. Lett. **115**, 142104 (2019).
24) G. Alfieri, V.K. Sundaramoorthy and R. Micheletto, J. Appl. Phys. **123**, 205303 (2018).
25) M. Akazawa, N. Yokota and K. Uetake, AIP Advances **8**, 025310 (2018).
26) M. Akazawa and K. Uetake, Jpn. J. Appl. Phys. **58**, SCCB10 (2019).
27) M. Akazawa, R. Kamoshida, S. Murai, T. Narita, M. Omori, J. Suda, and T. Kachi, Phys. Status Solidi B **256**, 1900367 (2019).
28) P. Hacke, T. Detchprohm, K. Hiramatsu, N. Sawaki, K. Tadatomo and K. Miyake, J. Appl. Phys. **76**, 304 (1994).
29) Z.-Q. Fang, D. C. Look, J. Jasinski, M. Benamara, Z. Liliental-Weber, R. J. Molnar, Appl. Phys. Lett. **78**, 332 (2001).
30) Z.-Q. Fang, D. C. Look, X.-L. Wang, J. Han, F. A. Khan, I. Adesida, Appl. Phys. Lett. **82**, 1562 (2003).
31) D. C. Look, G. C. Farlow, P. J. Drevinsky, D. F. Bliss, and J. R. Sizelove, Appl. Phys. Lett. **83**, 3525 (2003).
32) Y. Tokuda, Y. Matsuoka, H. Ueda, O. Ishigro, N. Soejima and T. Kachi, Superlattice and Microstructures **40**, 268 (2006).
33) A. R. Areheart, A. Corrion, C. Poblenz, J. S. Speck, U. K. Mishra, and S. A. Ringel, Appl. Phys. Lett. **93**, 112101 (2008).
34) U. Honda, Y. Yamada, Y. Tokuda and K. Shiojima, Jpn. J. Appl. Phys. **51**, 04DF04 (2012).
35) P. Kamyczek, E. Placzek-Popko, E. Zielony and Z. Zytkiewicz, Material Science-Poland **31**, 572 (2013).
36) A. Y. Polyakov, N. B. Smirnov, E. B. Yakimov, I.-H. Lee, and S. J. Pearton, J. Appl. Phys. **119**, 015103 (2016).
37) A. Uedono, S. Takashima, M. Edo, K. Ueno, H. Matsuyama, H. Kudo, H. Naramoto and S. Ishibashi, Phys. Status Solidi B **252**, 2794 (2015).
38) A. Uedono, S. Takashima, M. Edo, K. Ueno, H. Matsuyama, W. Egger, T. Koschine, C. Hugenschmidt, M. Dickmann, K. Kojima, S.F. Chichibu and S. Ishibashi, Phys. Status Solidi B **255**, 1700521 (2018).
39) A. Uedono, H. Iguchi, T. Narita, K. Kataoka, W. Egger, T. Koschine, C. Hugenschmidt, M. Dickmann, K. Shima, K. Kojima, S. F. Chichibu, and S. Ishibashi, Phys. Status Solidi B **256**, 1900104 (2019).

40) H. Iguchi, T. Narita, K. Kataoka, M. Kanechika, and A. Uedono, J. Appl. Phys. **126**, 125102 (2019).
41) A. van Veen, H. Schut, M. Clement, J. M. M. de Nijs, A. Kruseman, M. R. Ijpma, Appl. Surf. Sci. **85**, 216 (1995).
42) P. E. Blöchl, Phys. Rev. B **50**, 17953 (1994).
43) S. Ishibashi, T. Tamura, S. Tanaka, M. Kohyama, K. Terakura, Phys. Rev. B **76**, 153310 (2007).
44) S. F. Cagnina and E. H. Snow, J. Electrochem. Soc. **114**, 1165 (1967).
45) M. Miczek, B. Adamowicz, C. Mizue, and T. Hashizume, Jpn. J. Appl. Phys. **48,** 04C092 (2009).
46) S. M. Sze and K. K. Ng, *Physics of Semiconductor Devices* (Wiley, Hoboken, NJ, 2007) 3rd ed., Chap. 4.
47) H. Hasegawa and H. Ohno, J. Vac. Sci. & Technol. B **4**, 1130 (1986).
48) H. Hasegawa and M. Akazawa, Appl. Surf. Sci **254**, 8005 (2008).
49) T. Sawada, K. Numata, S. Tohdoh, T. Saitoh and H. Hasegawa, Jpn. J. Appl. Phys. **32**, 511 (1993).
50) T. Hashizume and R. Nakasaki, Appl. Phys. Lett. **80**, 4564 (2002).
51) S. Limpijumnong and C. G. Van de Walle, Phys. Rev. B **69**, 035207 (2004).
52) R. R. Wixom and A. F. Wright, Appl. Phys. Lett. **87**, 201901 (2005).
53) G. A. Umana-Membreno, J. M. Dell, G. Parish, B. D. Nener, L. Faraone, S. Keller, and U. K. Mishra, J. Appl. Phys. **101**, 054511 (2007).
54) F. Tuomisto, V. Ranki, D. C. Look, and G. C. Farlow, Phys. Rev. B **76**, 165207 (2007).
55) K. H. Chow, G. D. Watkins, A. Usui, and M. Mizuta, Phys. Rev. Lett. **85**, 2761 (2000).
56) G. Miceli and A. Pasquarello, Phys. Status Solidi PRL **11**, 1700081 (2017).
57) J. L. Lyons and C. G. Van de Walle, NPJ Computational Materials **12**, 1 (2017).

Figure Captions

Fig. 1. Schematic diagram of sample preparation sequence.

Fig. 2. Calculated and measured profiles for [Mg], [V_{Ga}] and [V_N].

Fig. 3. *C–V* characteristics of MOS diodes with the Mg ion dose of 1.5×10^{11} cm^{-2} annealed at (a) 300 ºC and (b) 500 ºC [experimental data in (a) is taken from Fig. 5(a) in Phys. Status Solidi B **256**, 1900367 (2019) with permission].

Fig. 4. D_T distribution evaluated from *C–V* characteristics for MOS diodes with Mg ion dose of 1.5×10^{11} cm^{-2} annealed at 300 ºC (solid circles) and 500 ºC (solid rectangles).

Fig. 5. *C–V* characteristics of MOS diodes with Mg ion dose of 1.5×10^{12} cm^{-2} annealed at (a) 300 ºC and (b) 500 ºC.

Fig. 6. *C–f* characteristics of MOS diodes with Mg ion dose of 1.5×10^{12} cm^{-2} annealed at (a) 300 ºC and (b) 500 ºC. A difference in color indicates a difference in bias voltage.

Fig. 7. G_p/ω extracted from *C–f* characteristics versus ω for samples with Mg ion dose of 1.5×10^{12} cm^{-2} annealed at (a) 300 ºC and (b) 500 ºC. A difference in color indicates a difference in bias voltage. Solid circles show experimental data, whereas solid lines are fitted lines according to single-time-constant model.

Fig. 8. D_T distribution evaluated from *C–f* characteristics for the samples with Mg ion dose of 1.5×10^{12} cm^{-2}.

Fig. 9. *S* as a function of incident positron energy for samples with Mg ion doses of (a) 1.5×10^{11} cm^{-2} and (b) 1.5×10^{12} cm^{-2}. Fine solid lines are fitting lines to the experimental data.

Fig. 10. *S* depth profiles obtained from the analysis of the *S–E* curves for the samples with doses of (a) 1.5×10^{11} cm^{-2} and (b) 1.5×10^{12} cm^{-2}. (The broken lines, the one-dot-chain lines, and the solid lines are for *S* for as-implanted, 300 ºC-annealed, and 500 ºC-annealed samples, respectively.) The depth profiles of the as-implanted Mg concentration measured by SIMS are also plotted by the solid circles.

Fig. 11. *S–W* relationship for samples with Mg ion doses of (a) 1.5×10^{11} cm^{-2} and (b) 1.5×10^{12} cm^{-2}. (*S, W*) values were measured at an incident positron energy of 5.1 keV. The brown DF data point indicates the result for the unimplanted GaN. The (*S, W*) values (blue) calculated using QMAS for positron annihilation in DF, V_{Ga}, $V_{Ga}(V_N)_n$ (n = 1–4), $(V_{Ga}V_N)_2$, $(V_{Ga}V_N)_3$, and $(V_{Ga})_2(V_N)_7$, are also plotted.

Fig. 12. D_T dependences of (a) $d\psi_S/dV$ and (b) C_{LF} calculated according to Eqs. (8) and (9), respectively.

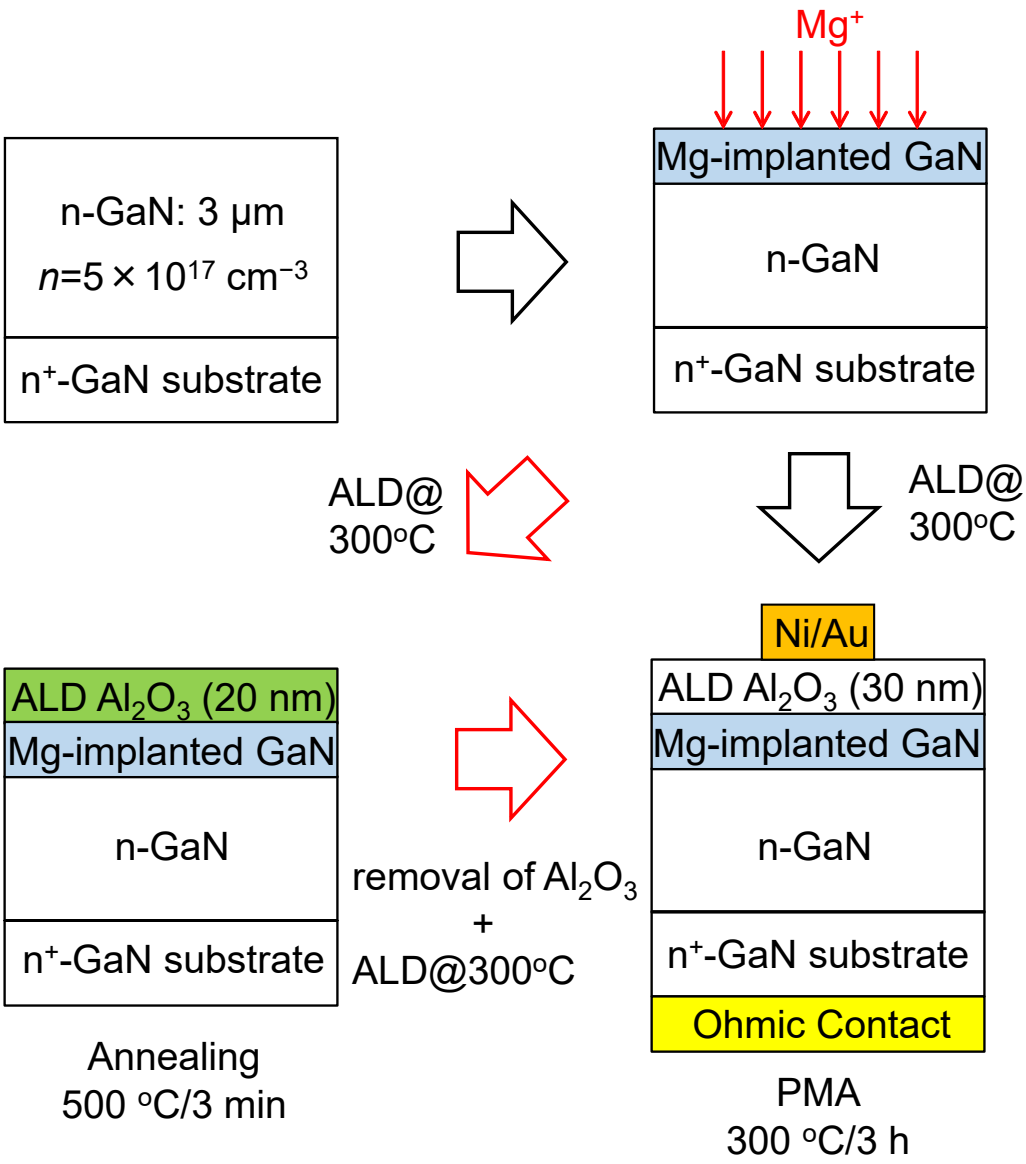
Mg+
n-GaN: 3 μm
n=5 × 10^17 cm^−3
n+-GaN substrate
Mg-implanted GaN
n-GaN
n+-GaN substrate
ALD@
300°C
ALD@
300°C
Ni/Au
ALD Al2O3 (20 nm)
Mg-implanted GaN
n-GaN
n+-GaN substrate
ALD Al2O3 (30 nm)
Mg-implanted GaN
n-GaN
n+-GaN substrate
Ohmic Contact
removal of Al2O3
+
ALD@300°C
Annealing
500 °C/3 min
PMA
300 °C/3 h

Fig.1.

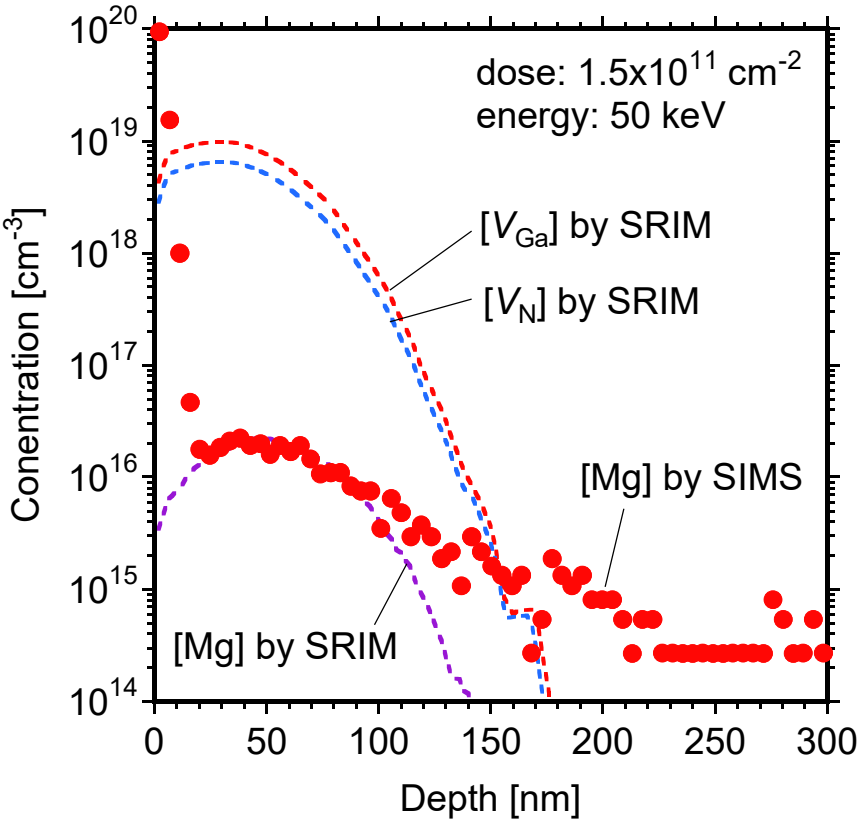
dose: 1.5x10^11 cm^-2
energy: 50 keV
[V_Ga] by SRIM
[V_N] by SRIM
[Mg] by SIMS
[Mg] by SRIM
Conentration [cm^-3]
Depth [nm]
10^20
10^19
10^18
10^17
10^16
10^15
10^14
0
50
100
150
200
250
300

Fig. 2

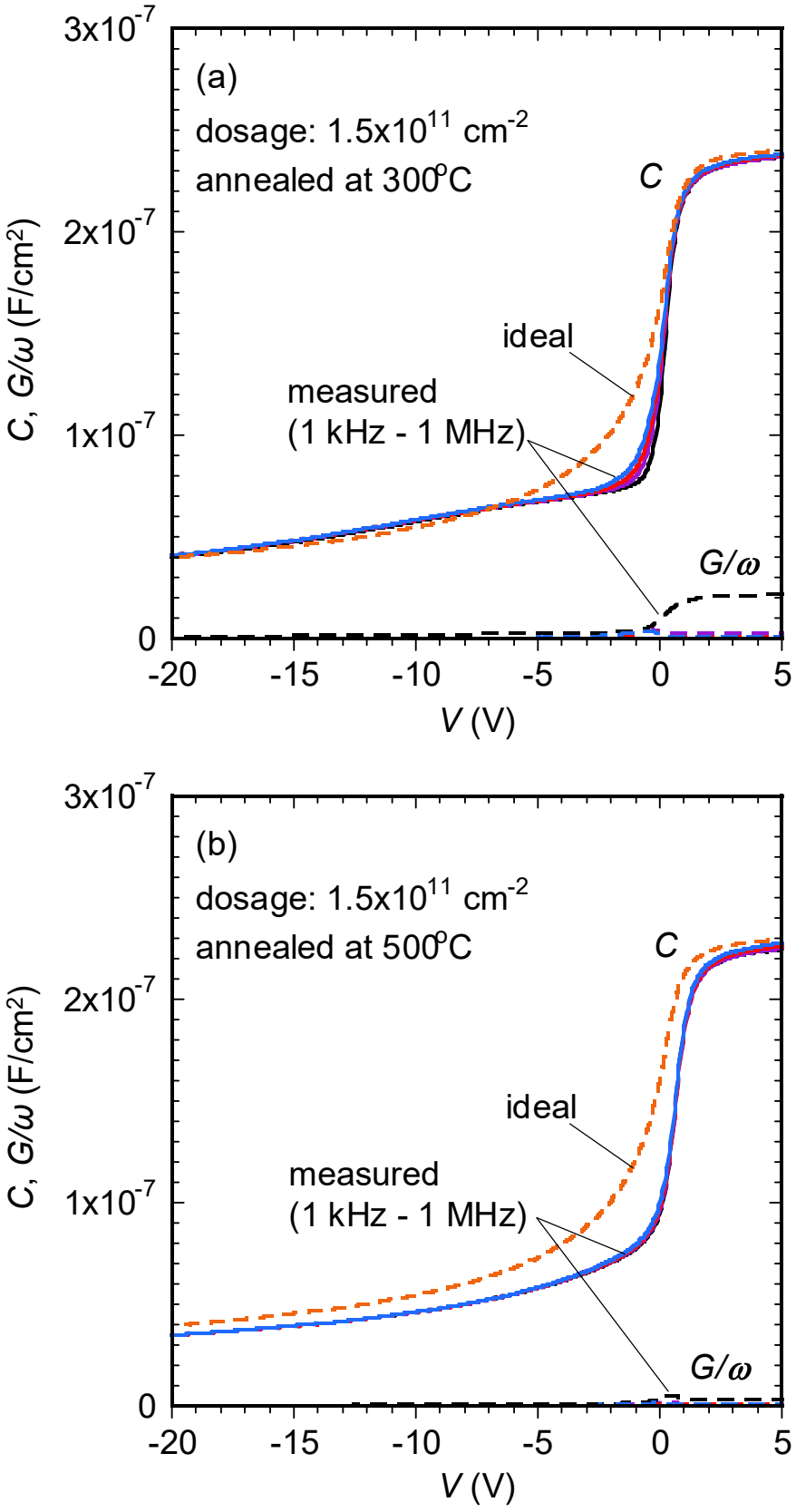
(a)
dosage: 1.5x10^11 cm^-2
annealed at 300°C
C
ideal
measured
(1 kHz - 1 MHz)
G/ω
C, G/ω (F/cm²)
V (V)
(b)
dosage: 1.5x10^11 cm^-2
annealed at 500°C
C
ideal
measured
(1 kHz - 1 MHz)
G/ω
C, G/ω (F/cm²)
V (V)

Fig. 3

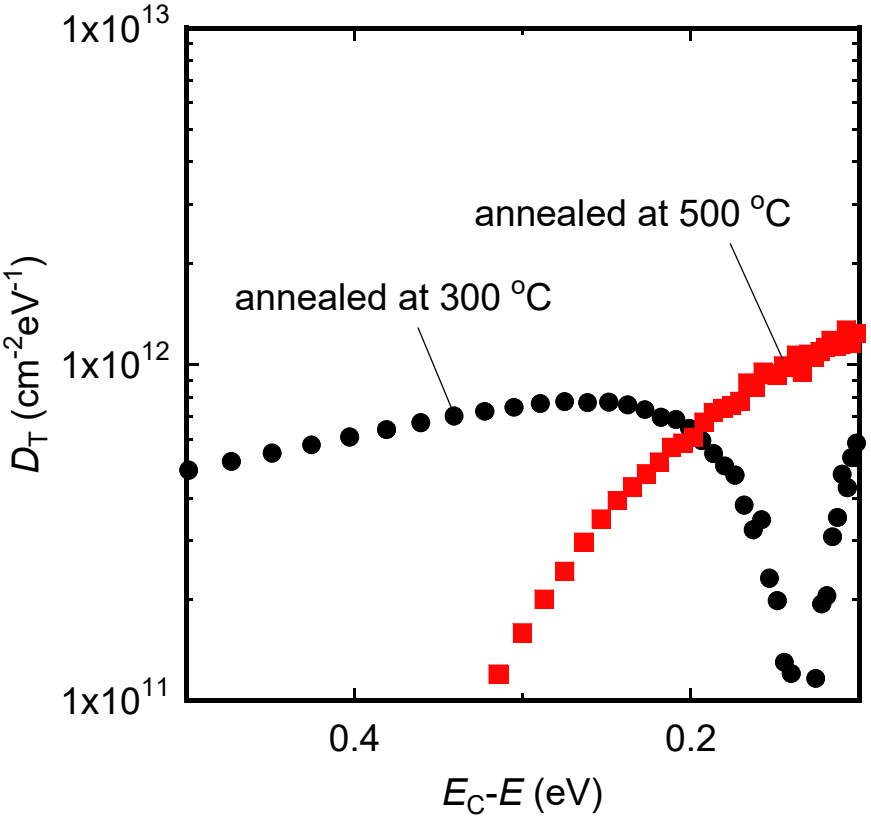
1x10^13
1x10^12
1x10^11
D_T (cm^-2eV^-1)
annealed at 500 °C
annealed at 300 °C
0.4
0.2
E_C-E (eV)

Fig. 4

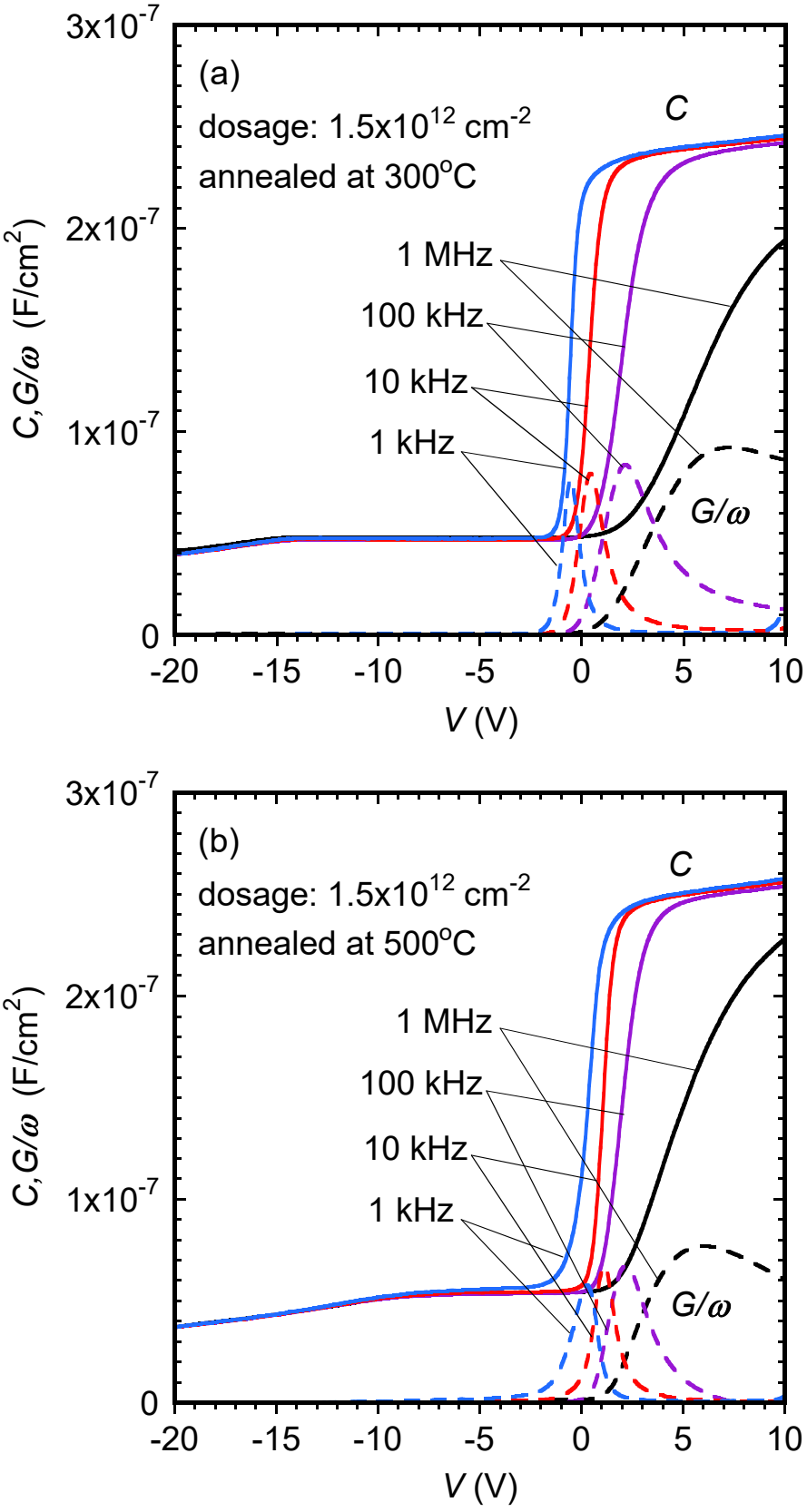
(a)
dosage: 1.5x10^12 cm^-2
annealed at 300°C
C
1 MHz
100 kHz
10 kHz
1 kHz
G/ω
C,G/ω (F/cm^2)
V (V)
(b)
dosage: 1.5x10^12 cm^-2
annealed at 500°C
C
1 MHz
100 kHz
10 kHz
1 kHz
G/ω
C,G/ω (F/cm^2)
V (V)

Fig. 5

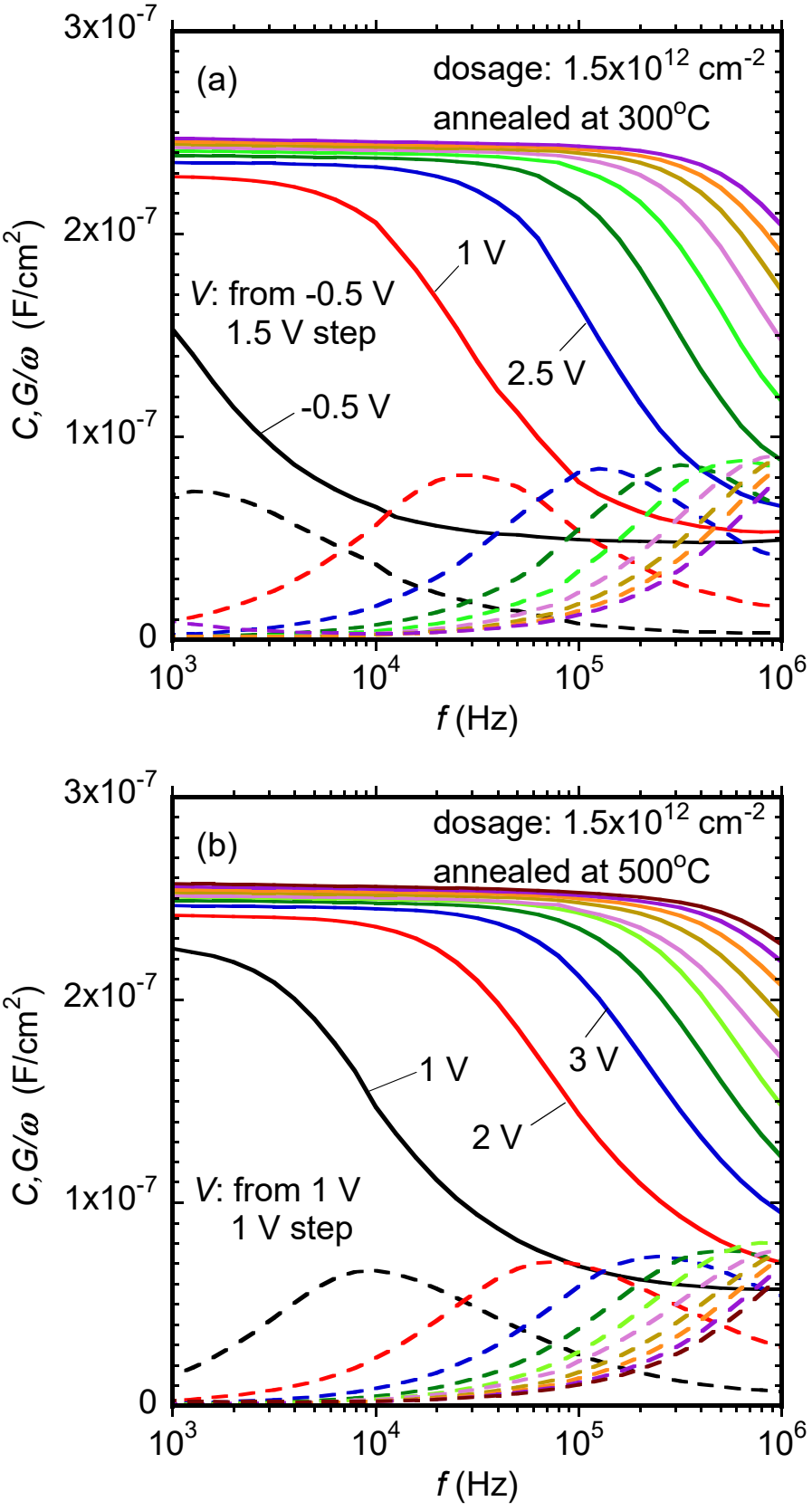
(a)
dosage: 1.5x10^12 cm^-2
annealed at 300°C
V: from -0.5 V
1.5 V step
1 V
2.5 V
-0.5 V
C,G/ω (F/cm^2)
f (Hz)
(b)
dosage: 1.5x10^12 cm^-2
annealed at 500°C
V: from 1 V
1 V step
1 V
2 V
3 V
C,G/ω (F/cm^2)
f (Hz)

Fig. 6

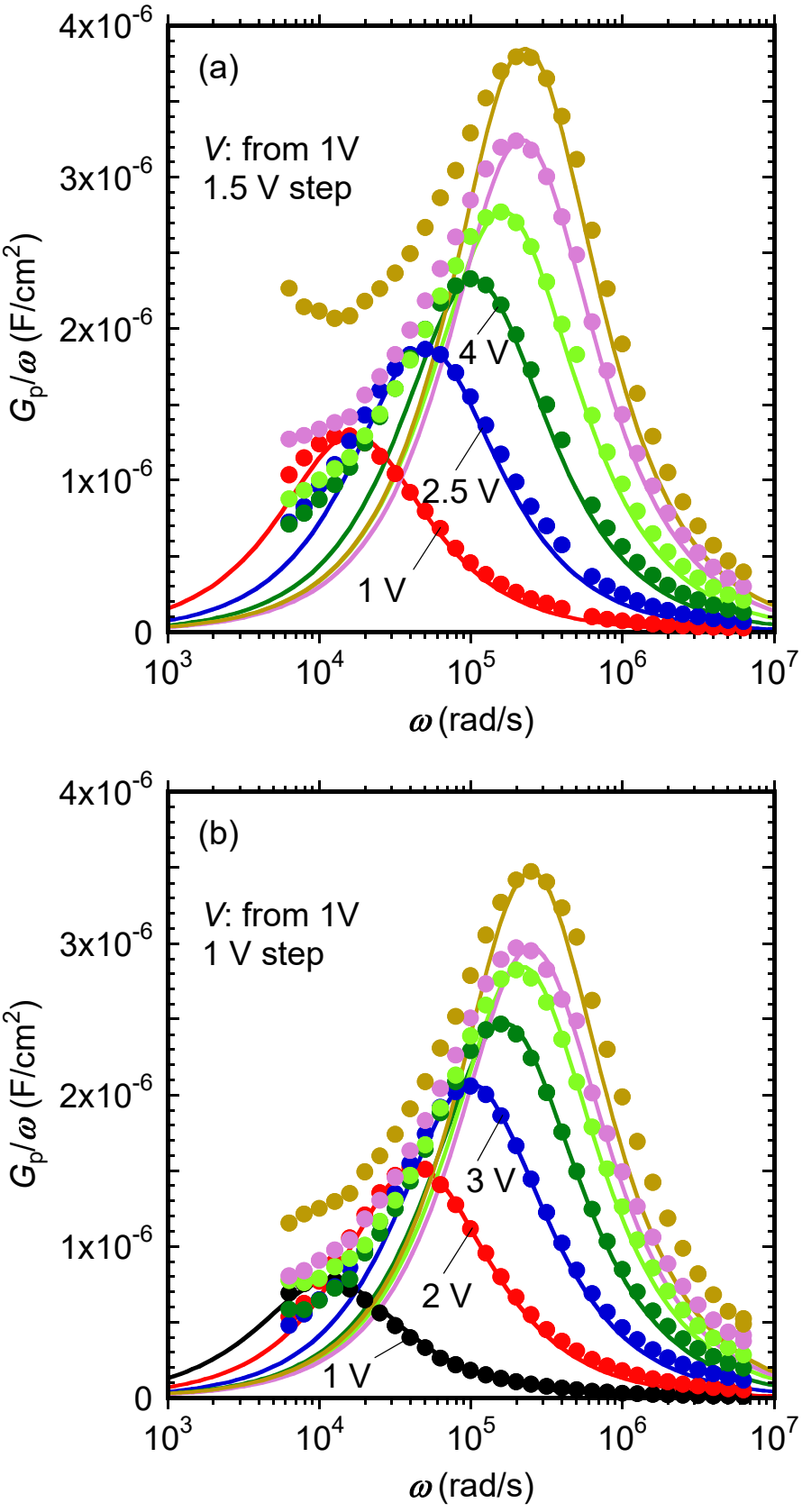
(a)
V: from 1V
1.5 V step
4 V
2.5 V
1 V
(b)
V: from 1V
1 V step
3 V
2 V
1 V
G_p/ω (F/cm^2)
ω (rad/s)
4x10^{-6}
3x10^{-6}
2x10^{-6}
1x10^{-6}
0
10^3
10^4
10^5
10^6
10^7

Fig. 7

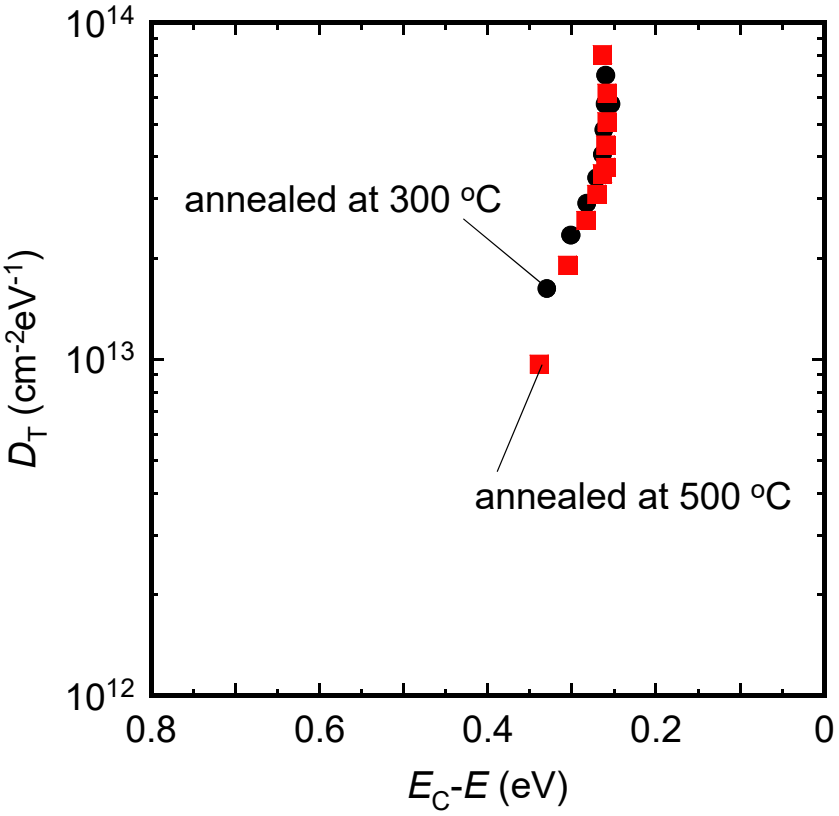
10^{14}
10^{13}
10^{12}
D_T (cm^{-2}eV^{-1})
annealed at 300 °C
annealed at 500 °C
0.8
0.6
0.4
0.2
0
E_C-E (eV)

Fig. 8

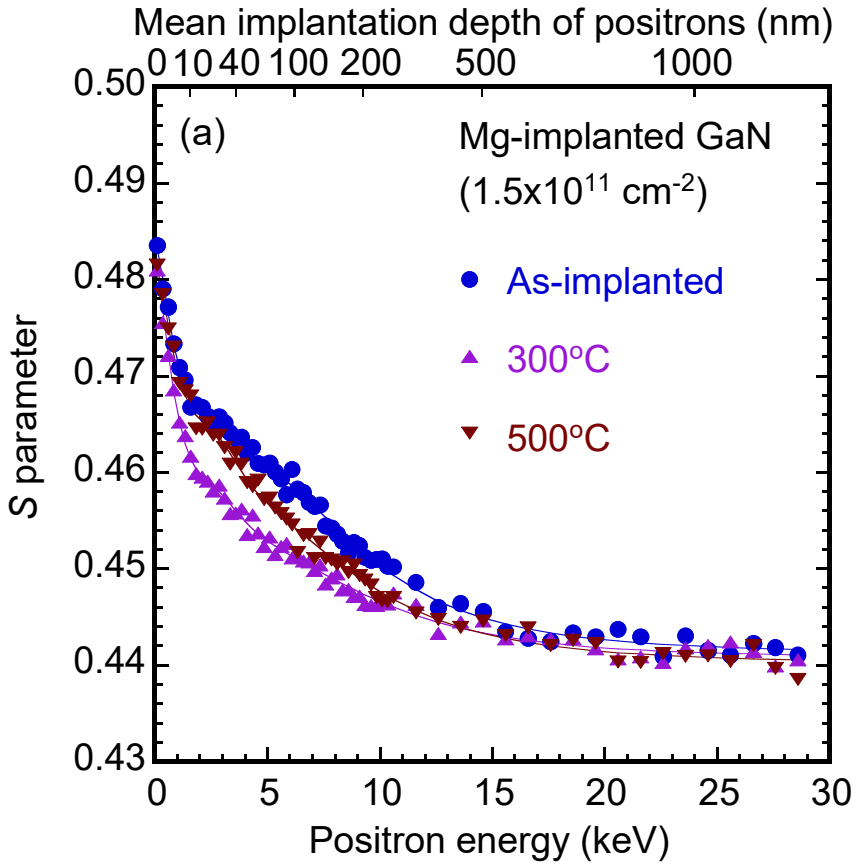
Mean implantation depth of positrons (nm)
0 10 40 100 200 500 1000
(a)
Mg-implanted GaN
(1.5x10^11 cm^-2)
As-implanted
300°C
500°C
S parameter
Positron energy (keV)

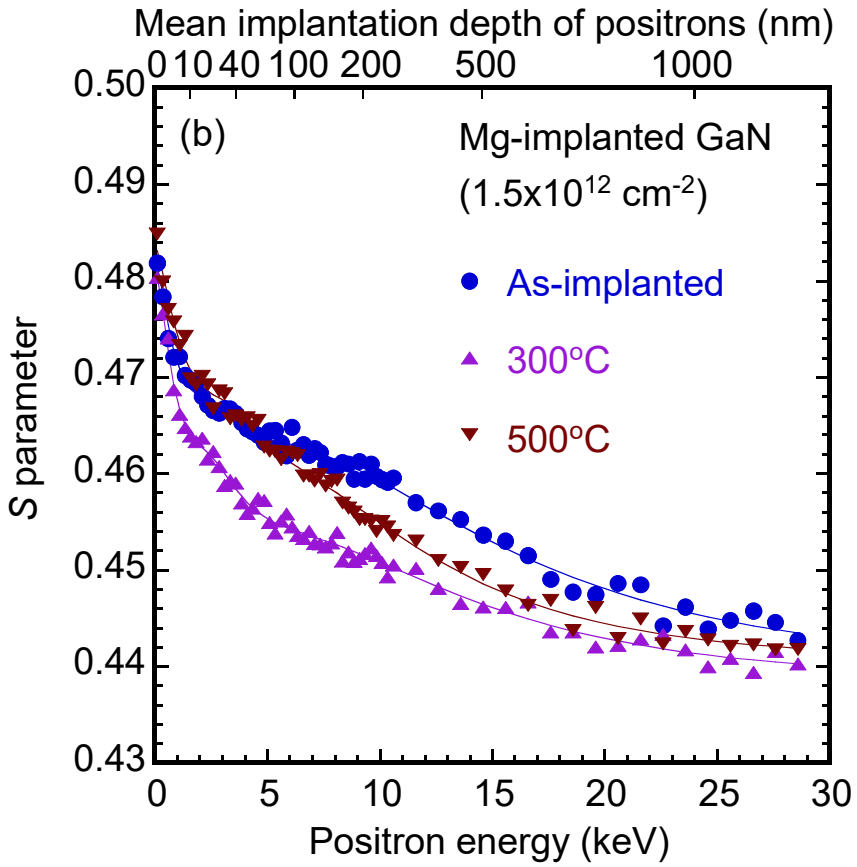
Mean implantation depth of positrons (nm)
0 10 40 100 200 500 1000
(b)
Mg-implanted GaN
(1.5x10^12 cm^-2)
As-implanted
300°C
500°C
S parameter
Positron energy (keV)

Fig. 9

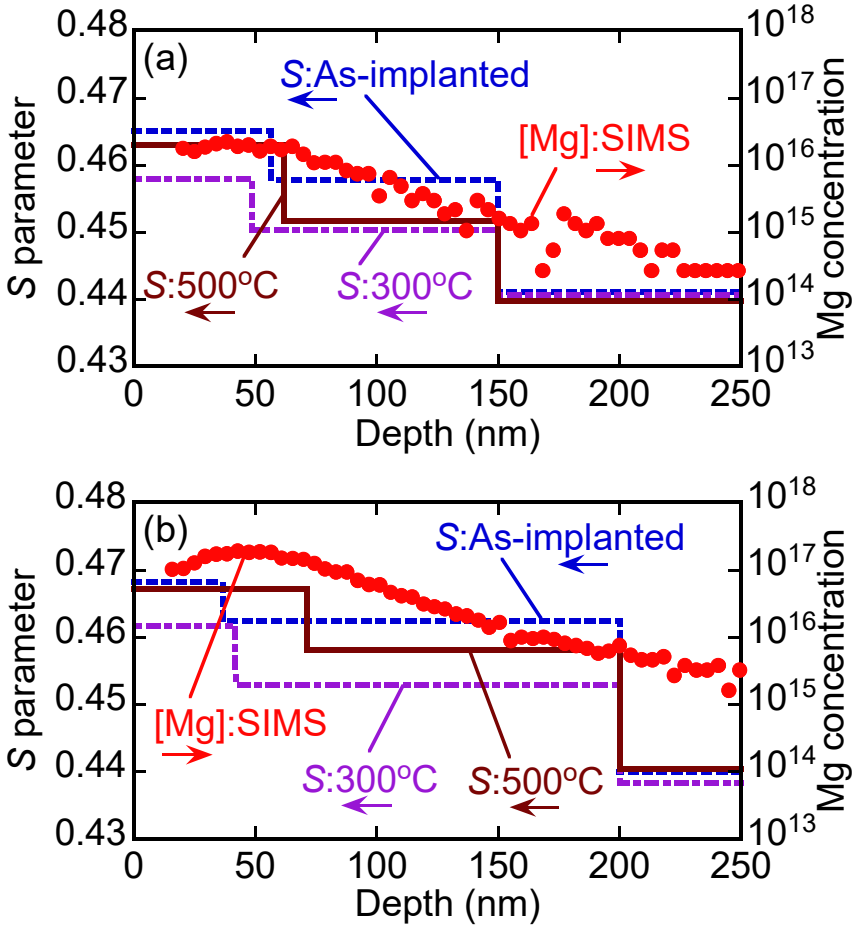
(a)
S:As-implanted
[Mg]:SIMS
S:500°C
S:300°C
S parameter
Mg concentration
Depth (nm)
(b)
S:As-implanted
[Mg]:SIMS
S:300°C
S:500°C
S parameter
Mg concentration
Depth (nm)

Fig. 10

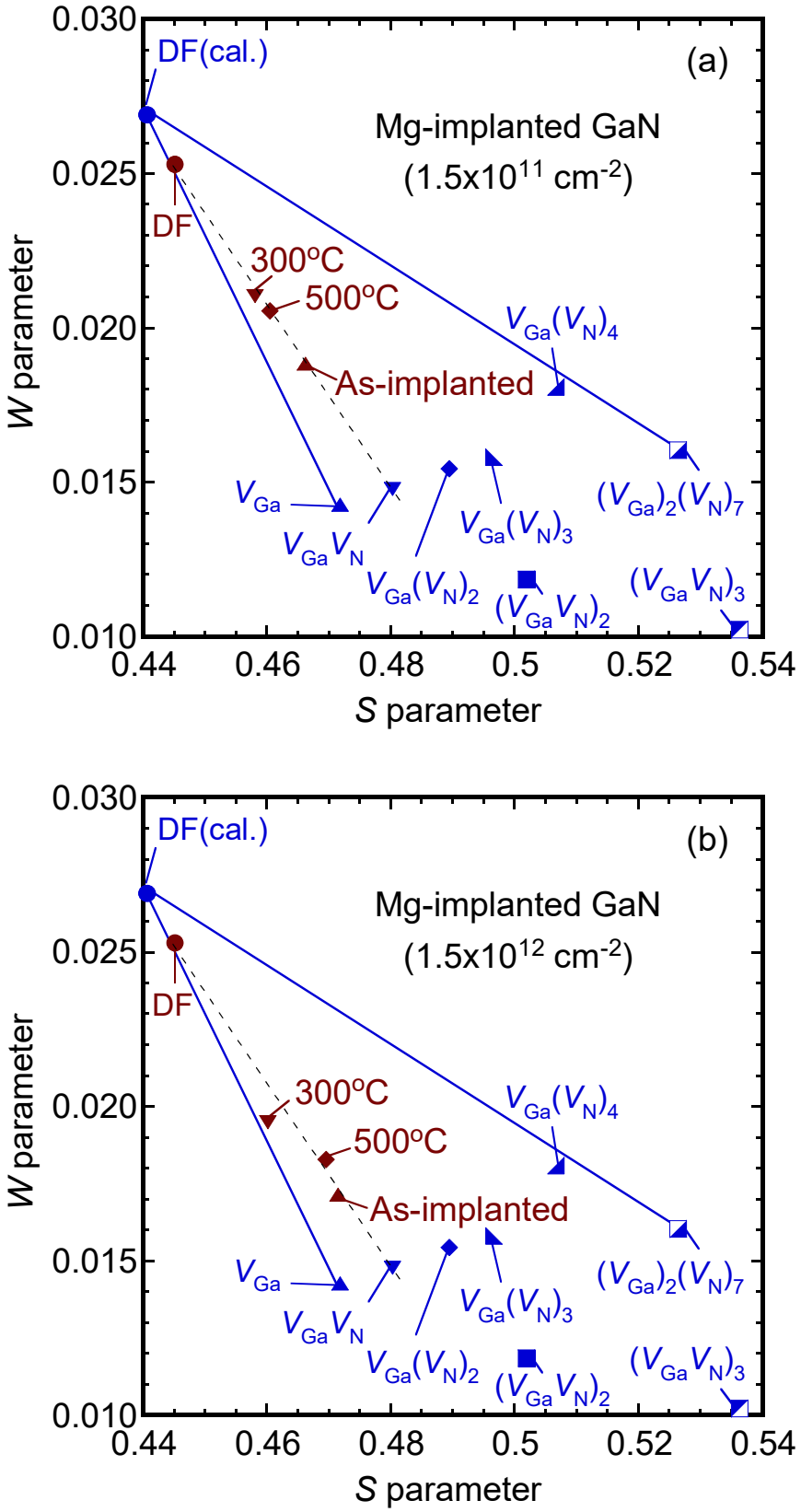
(a)
Mg-implanted GaN
(1.5x10^11 cm^-2)
DF(cal.)
DF
300°C
500°C
As-implanted
V_Ga(V_N)_4
V_Ga
V_Ga V_N
V_Ga(V_N)_2
V_Ga(V_N)_3
(V_Ga)_2(V_N)_7
(V_Ga V_N)_2
(V_Ga V_N)_3
W parameter
S parameter
0.030
0.025
0.020
0.015
0.010
0.44
0.46
0.48
0.5
0.52
0.54
(b)
Mg-implanted GaN
(1.5x10^12 cm^-2)
DF(cal.)
DF
300°C
500°C
As-implanted
V_Ga(V_N)_4
V_Ga
V_Ga V_N
V_Ga(V_N)_2
V_Ga(V_N)_3
(V_Ga)_2(V_N)_7
(V_Ga V_N)_2
(V_Ga V_N)_3
W parameter
S parameter

Fig. 11

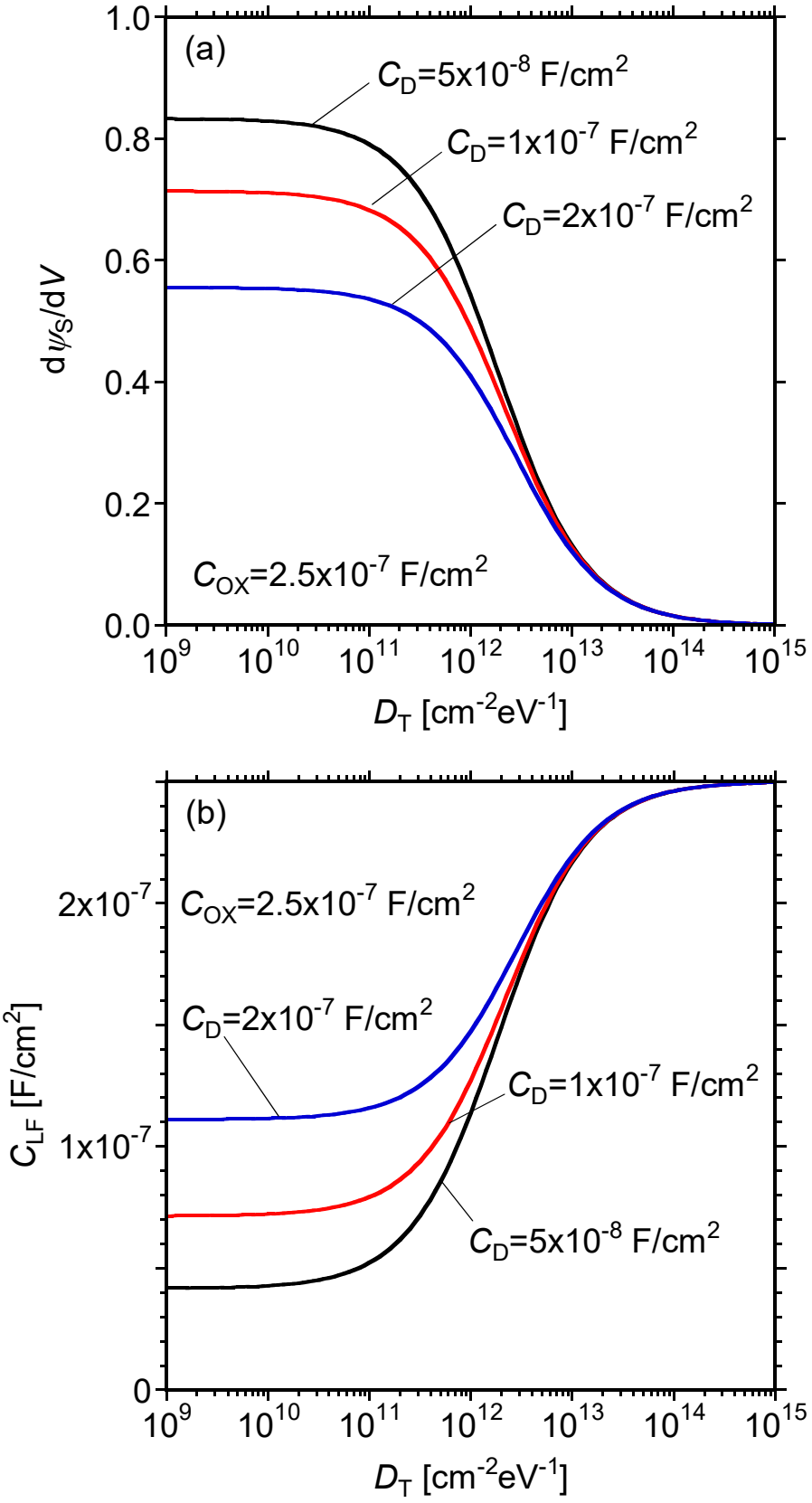
(a)
C_D=5x10^{-8} F/cm^2
C_D=1x10^{-7} F/cm^2
C_D=2x10^{-7} F/cm^2
C_{OX}=2.5x10^{-7} F/cm^2
dψ_S/dV
D_T [cm^{-2}eV^{-1}]
(b)
C_{OX}=2.5x10^{-7} F/cm^2
C_D=2x10^{-7} F/cm^2
C_D=1x10^{-7} F/cm^2
C_D=5x10^{-8} F/cm^2
C_{LF} [F/cm^2]
D_T [cm^{-2}eV^{-1}]

Fig. 12